JOURNAL OF PROPULSION AND POWER
Vol. 10, No. 5, Sept.–Oct. 1994

Calculation of Scramjet Inlet with Thick Boundary-Layer Ingestion

Hien T. Lai* and Suk C. Kim*
Sverdrup, Inc., Brook Park, Ohio 44142
and
Henry T. Nagamatsu†
Rensselaer Polytechnic Institute, Troy, New York 12180

Numerical flowfields around a scramjet inlet model are simulated and analyzed. The present inlet flowfield is characterized by thick boundary-layer ingestion, strong viscous and inviscid interaction due to the combined effect of high Mach number and low Reynolds number, and shock-induced separation that enlarges regions of viscous flows. Results obtained from the computations with a full Navier-Stokes code are presented for several two-dimensional cases at Mach number ranging from 10 to 14.9, and one three-dimensional case at Mach number of 12. Comparison between computation and experiment is made in terms of pressure distributions at the wall centerline. Large discrepancy is observed and may be partially attributed to the lack of real gas and/or three-dimensional effects in the simulation, as well as to the uncertainty of the experiment.

Introduction

SEVERAL computational studies of the flowfields around scramjet inlets have been conducted in the regime of high Reynolds numbers Re and low hypersonic Mach numbers[1,2] M_∞. The flow in such cases remains primarily inviscid, and the viscous effects are limited to thin boundary layers along the inlet walls. In contrast, for flows at low Reynolds and high Mach numbers, which correspond to the high-altitude operating conditions of a scramjet engine, the boundary layers thicken to a considerable extent of the inlet aperture, causing a severe nonuniform flow that must be ingested by the inlet. There are also other physical features that are frequently encountered in high-speed flows, especially in the inlet configuration. At hypersonic Mach numbers, there exist regions of strong viscous/inviscid interaction near the inlet leading edges, possibly creating merged regions of oblique shocks and boundary layers. Shock/shock crossing, shock impingement, and shock-induced separation are other examples of common flow structures present in the inlet. Another important characteristic of hypersonic engines is the complex coupling between internal and external flows since part of the engine is integrated with the airframe.

The computations presented here are performed to simulate the flowfields of an inlet model that has been studied experimentally[3,4] in a hypersonic shock-tube tunnel using dry air as test gas. A series of test cases were investigated in the experiment corresponding to two flow conditions referred to as low and high enthalpy runs with stagnation temperatures of 1100 and 4000 K, respectively. The present work attempts to numerically reproduce the experimental flowfields only for the low enthalpy case to avoid modeling the real gas effects at high temperature. Even at this low temperature, real gas effects may exist and the Knudsen number can also be large near the inlet leading edge, making the assumption of continuum flows no longer valid. Since these physical features are not represented in the present computational model, the solution accuracy is therefore degraded in the regions where their influences are dominant. However, computed flowfields neglecting these effects can still provide useful and essential information about the primary characteristics of the flowfield in a hypersonic inlet.

Numerical flowfields are computed with the PARC code, which has been extensively validated for various flowfields of many practical configurations. Particularly for high-speed inlets and nozzles, laminar and turbulent results have recently been documented for flows at supersonic and hypersonic Mach numbers.[1,5–7] This article is also intended to illustrate another computational fluid dynamics (CFD) validating case for the PARC code as a part of the continuing efforts to apply the CFD methods to calculate the complex high-speed flowfields. Several cases with Mach number ranging from 10 to 14.9 are calculated with a two-dimensional model representing the symmetric plane of the scramjet engine. The corresponding freestream unit Reynolds numbers are in the order 1×10^6. Both laminar and turbulent cases are computed to compare the characteristics of the shock wave/boundary-layer interaction leading to separation. A grid study is also conducted for the two-dimensional configuration to achieve grid-independent solutions. Finally, computations for the laminar flow at the Mach number of 12 are performed for the three-dimensional model to investigate any three-dimensional effects that may be present.

Numerical Method

The finite difference PARC code[8,9] is employed to solve the full Navier-Stokes equations in a generalized curvilinear-coordinate system. Standard central differences are used for discretization of the governing equations, and Jameson-type artificial damping is added to avoid nonphysical oscillation and to provide stability. The implicit inviscid terms are diagonalized for computational efficiency, and the resulting linearized algebraic equations are solved using the Beam-Warming ADI algorithm. In a time-like marching manner, the solutions are iterated from an initial guess with variable time steps to obtain quick convergence to a steady state. The code has the capability to handle a broad class of complex geometries with a single grid by dividing the domain into several patches, based on surface contours' definition, without requiring special treatments at the patch interface. This ad-

Received Aug. 14, 1993; revision received Jan. 31, 1994; accepted for publication Feb. 12, 1994.

*Senior Research Engineer, 2001 Aerospace Parkway. Member AIAA.

†Active Professor Emeritus of Aeronautical Engineering. Fellow AIAA.

vantage can be utilized to simulate a complete numerical flowfield closely representative of the experiment with less complication.

Turbulent flows are calculated with a modified Baldwin-Lomax model[9,10] designed to simulate general flowfields containing various viscous phenomena in which multiple length scales may exist, e.g., as in flows with boundary layers and mixing shear layers. Results consistent with experiments have been obtained using the model for low supersonic Mach numbers.[1,6] However, the model's poor behavior has been experienced for hypersonic Mach numbers,[7] especially in the region of shock wave/boundary-layer interaction. The discrepancy is largely caused by the lack of compressibility effect that has not been taken into account when formulating the model. Therefore, results discussed here are only qualitatively meaningful with possible improvements if a compressibility correction can be incorporated.

For boundary conditions, all far-field dependent variables are fixed to the undisturbed freestream values, provided that they are imposed at a distance sufficiently far from the inlet model. A uniform hypersonic profile is prescribed at the inflow boundary and extrapolation is used at the outflow boundary. No-slip velocities and isothermal temperatures are specified on the solid walls.

Geometry and Grid

The scramjet engine model tested in the experiment is schematically illustrated in Fig. 1, consisting simply of a long lower centerbody, which is usually integrated as an undersurface of the aerospace vehicle, and an upper cowl designed relatively short in length to reduce the vehicle's weight. These two surfaces form an inlet comprising of a compression ramp extending slightly beyond the sharp cowl lip, and a straight duct passage ending at the cowl blunt trailing edge and the centerbody second expansion corner. The arrangement also allows for an exhaust flow in the rear section, representing a typical scramjet nozzle using part of the centerbody as its only expanding surface. There is no sidewall along the duct passage so that the flow can freely expand toward and spill over the edges of the model because of pressure imbalance between internal and ambient flows, contributing to the three-dimensional relieved effect.

The coordinate system is selected with x, y, and z axes oriented in the streamwise, vertical, and spanwise directions, respectively, and with an origin placed at the ramp leading edge in the symmetric plane, as shown in Fig. 1. All dimensions indicated are in millimeters. The computational grids are shown in Fig. 2 for the fully three-dimensional model, and in Fig. 3 for the two-dimensional symmetry plane. In Fig. 2, the grid is shown for the cowl surface, the center body, and some segments of the computational boundaries. It can be seen that the upper boundary grid line is chosen to closely align with the highly inclined external shocks emerging from

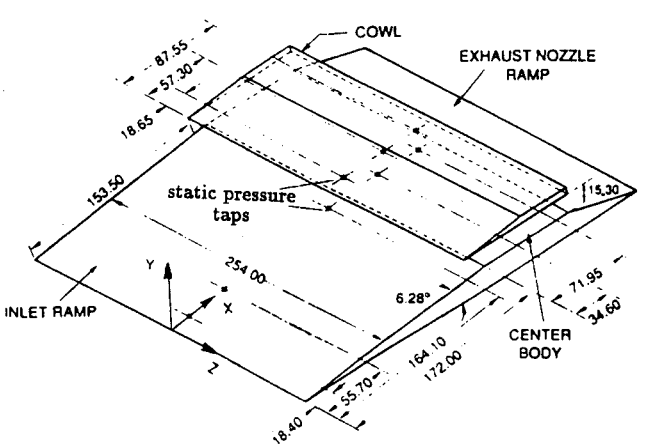

Fig. 1 Scramjet engine model (all dimensions in mm).

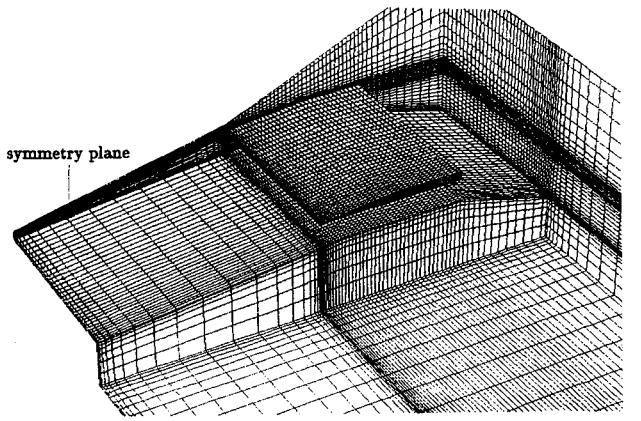

Fig. 2 Three-dimensional grid distribution.

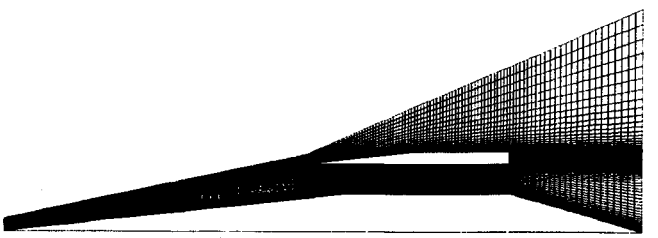

Fig. 3 Two-dimensional grid distribution.

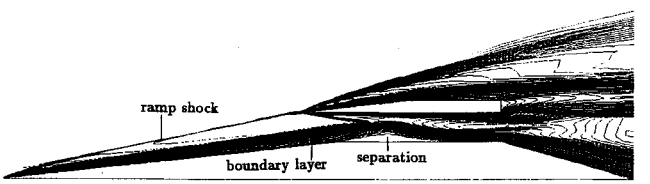

Fig. 4 Mach number contours, laminar, $M = 12$.

the ramp and cowl's sharp leading edges. In the flow direction, grid refinement is prescribed primarily near the cowl lip to capture shock crossing and/or the cowl internal shock, and along the duct passage to resolve the expected flow separation, shock impingements, and shock reflections. For the region behind the cowl's blunt trailing edge, the flow is complex involving viscous-dominated flows in a wake, then followed by a mixing shear layer occurring between two hypersonic streams. This region is simulated, but only for completeness since the exhaust flow may have a negligible upstream influence through the thin subsonic zone of the viscous layer and there is no experimental data for comparison in this region. For the fully three-dimensional model, the grid is generated by stacking the two-dimensional x-y grid in the spanwise direction. Since the external freestream flow adjacent to the sidewall is included as a part of the computational domain, the secondary crossflows caused by the spanwise spillage effect can be captured. Only half of the model is computed using the symmetry plane as one of the two spanwise boundaries.

Results

Computations are performed for the two-dimensional model at four different freestream Mach numbers, $M_\infty = 10.1$, 12, 13.2, and 14.9. The corresponding freestream pressure and temperature are $P_\infty = 39$, 12, 6.3, and 4.4 Pa, and $T_\infty = 36.3$, 26.6, 22.2, and 20.8 K. The computed freestream unit Reynolds numbers are, accordingly, $Re = 2.1 \times 10^6$, 1.4×10^6, 1.1×10^6, and 9.2×10^5/m. A wall temperature of 299 K is prescribed at the solid surface. All cases are computed with a 145 × 125 grid.

A typical laminar flowfield of the present scramjet engine is shown in Figs. 4 and 5 in terms of Mach number and pressure contours for a freestream Mach number of 12. It can be

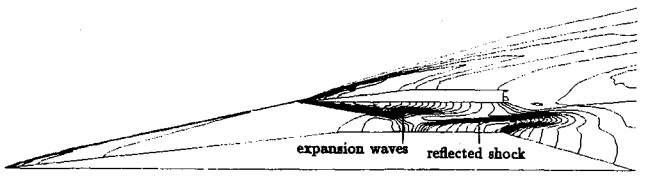

Fig. 5 Pressure contours, laminar, $M = 12$.

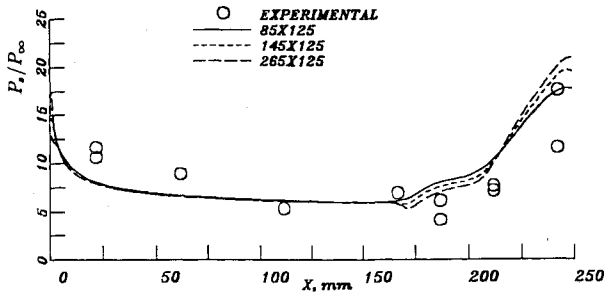

Fig. 6 Centerbody pressure, refinement in x direction.

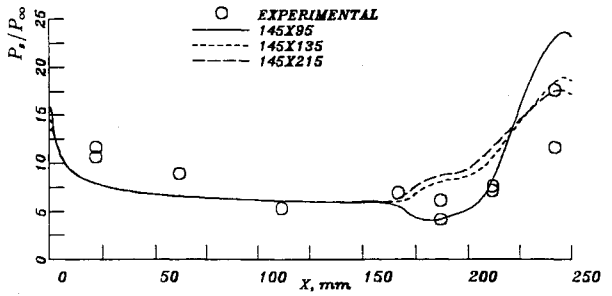

Fig. 7 Centerbody pressure, refinement in y direction.

seen that oblique shock waves and thick viscous layers are prominent features of the overall flowfield. The boundary layer along the ramp surface is quite substantial and its thickness is more than half the height of the duct passage as shown in Fig. 4. Downstream of the expansion corner, the boundary layer becomes thicker and then separates because of its interaction with the cowl internal shock, leaving a very narrow inviscid region within the duct passage. Wave structure around the separation can be seen more clearly from the pressure contours in Fig. 5, identified by a large interaction zone with expansion waves immediately above the separation bubble and a nearly horizontal shock reflection downstream. As indicated by the dense contours, the reflection does not intersect the cowl, but passes through the plane of the nozzle entrance in the middle, to be dissipated by the exhaust flow.

The ramp shock also does not impinge on the cowl's internal surface, but passes slightly above the cowl lip, causing an expansion flow around the cowl leading edge on the external surface. Consequently, the shock wave is perturbed by the expansion and deflected at a larger angle, eventually becoming more and more diffused because of grid coarseness.

A grid study is conducted for the two-dimensional laminar flow at $M_\infty = 12$, and results for wall pressure along the symmetry plane are presented in Figs. 6–8. The purpose is to examine how far the grid needs to be resolved to achieve grid-independent solutions. The grids in Figs. 6 and 7 are separately refined in the the x and y directions, and the grid in Fig. 8 is refined in both directions. The refinement is done by doubling the number of grid points only in regions where the results can be compared with experiments, i.e., the flows along the ramp and in the duct passage. Downstream of the cowl's trailing edge, the flow is mostly supersonic, thus the solutions at these regions do not affect the solutions along the ramp and inside the duct significantly.

In Figs. 6–8, the wall pressure is plotted from the ramp leading edge to the end of the duct passage. Large discrepancy

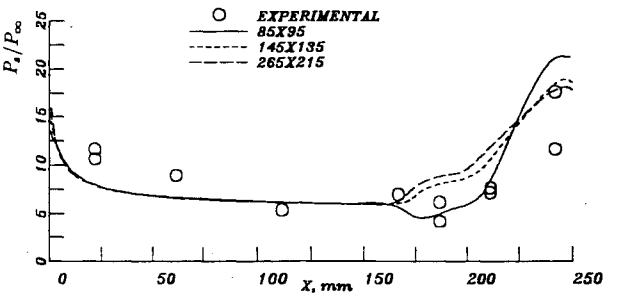

Fig. 8 Centerbody pressure, refinement in both directions.

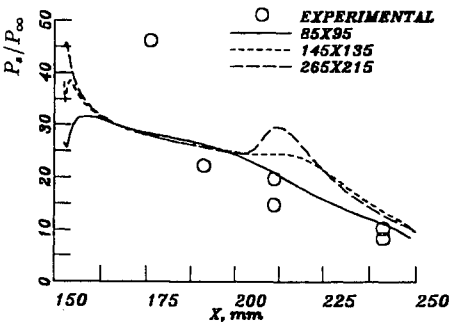

Fig. 9 Cowl pressure distributions.

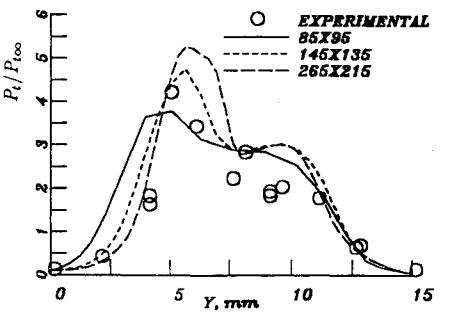

Fig. 10 Duct passage pressure profiles at $x = 25$ cm.

between computation and experiment occurs near the leading edge and in the separation region. While there is large disagreement between the present solutions and the experimental data near the leading edge and it can lead to further deterioration of the solution downstream, the calculated wall pressure near the end of the inlet ramp agrees relatively well with the experimental data. The large difference between the present results and the experimental data near the leading edge may be due to the numerical and/or experimental uncertainty, but cannot be explained in the present study. Grid refinement the x direction slightly improves the separation point, but gives a stronger pressure rise, as shown in Fig. 6, leading to a smaller separation bubble. On the other hand, refinement in the y direction has an opposite effect that moves the separation point upstream and enlarges the bubble size as seen from Fig. 7. It can be observed that increasing grid resolution in the y direction has a larger effect on the solution than refinement in the x direction. This observation is more evident in Fig. 8, where refinement in both directions shows a pattern of pressure distributions similar to that of the refinement in the y direction.

In Fig. 8, there is an indication that the results converge when the grid is refined. At the interaction, it appears that the pressure distribution on the coarse grid is in better agreement with the measured data. However, this agreement is misleading since the interaction zone with or without separation is not accurately resolved but suppressed to develop by numerical viscosity. This coarse-grid solution resembles the turbulent results, discussed below, in which the interaction zone is instead affected by physical turbulent viscosity. The

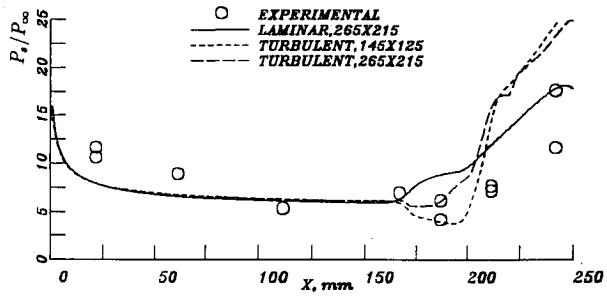

Fig. 11 Centerbody pressure, laminar and turbulent, $M = 12$.

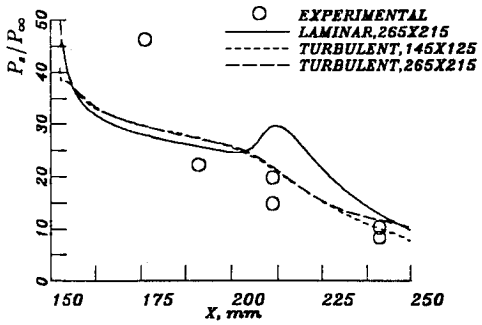

Fig. 12 Cowl pressure, laminar and turbulent, $M = 12$.

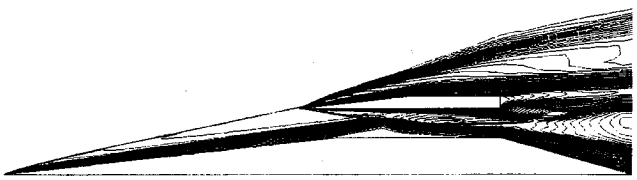

Fig. 13 Mach number contours, laminar, 265 × 215, $M = 12$.

Fig. 14 Mach number contours, turbulent, 265 × 215, $M = 12$.

fine-grid distributions still represent more accurate solutions of the governing equations, although the results do not agree with the experiment. Other factors must be examined to explain the discrepancy associated with fine grids.

In general, there is some improvements when the grid size is reduced, but none of the grids seems to give a satisfactory result near the separation. Figures 9 and 10 show the wall pressure distributions on the cowl's internal surface along the symmetric plane and a pitot pressure across the duct passage at the cowl's blunt trailing edge, respectively. The pitot pressure presents a description of a flow structure across the duct that is determined largely by the upstream flow, especially by the reflected shock and the expansion waves emerging at the separation. For the fine grid resolution, the result indicates a second impingement of yet another shock wave on the cowl surface, shown in Fig. 9 as a small pressure hump at about $x = 210$ mm, that is not observed in the experiment. This shock, referred to as separation shock in Refs. 3 and 4, is a result of the complex flow pattern near the shock wave/boundary-layer interaction, and is present when the streamline around the separated bubble is rapidly lifted up due to a severe shock impingement. It appears that only very fine grids, particularly in the y direction, can capture the separation shock. The trend, however, is misleading since the figure suggests a better agreement for the coarse grid solution without impingement. The differences among the data are particularly more pronounced for the pitot pressure distributions depicted in Fig. 10, varying widely and showing no obvious solution convergence as the grid is refined. The reason for this observation is that the solution here is not only dependent of the grid alone but also highly of the upstream solution that must be predicted accurately. Turbulent flows are computed with two different grids for $M_\infty = 12$, and results are shown in Figs. 11 and 12. Large discrepancy between the numerical solutions and the experimental data is again observed at the shock wave/boundary-layer interaction region. Computed turbulent results exhibit a pressure drop across the first corner of the centerbody and give a better agreement with measured data for the cowl pressure distributions on either grid as seen from these figures. As mentioned earlier for the laminar flows, refining the grid in turbulent flows also increases the upstream influence, and consequently reduces the expansion effect of the corner because of boundary-layer thickening or separation. It is noted that the turbulent pressure variation on the ramp near the corner is similar to those obtained for the laminar flows with the coarse grids in Figs. 7 and 8. In turbulent flows, the interaction zone is weakened by the effect of eddy viscosity.

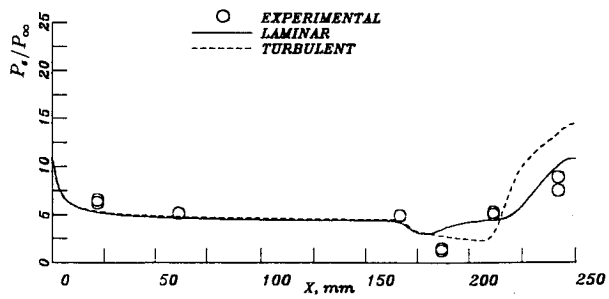

Fig. 15 Centerbody pressure, 145 × 125, $M = 10.1$.

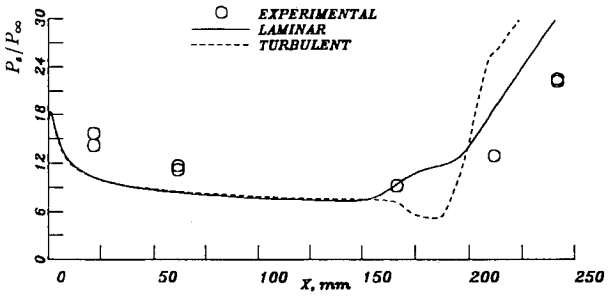

Fig. 16 Centerbody pressure, 145 × 125, $M = 13.2$.

Mach number contours for laminar and turbulent flows with a 265 × 215 are shown in Figs. 13 and 14. The thickness of the ramp boundary layer in both flows remains nearly the same upstream of the corner. Near and downstream of the interaction there are significant changes in the extent of the viscous regions, with a smaller separated bubble for the turbulent flows. In Fig. 13 evidently the streamlines are deflected above the bubble to alter the effective body curvature. Although it cannot be visualized clearly here, the shifting of the streamlines are more abrupt and severe immediately at the impingement, allowing the separation shock to form. In the turbulent case, the streamlines are smoother at the impingement so that the shock degenerates into compression waves. In a similar manner with the flow downstream, the reflected shock in the turbulent flow is also dissipated into weak compression waves, occurring earlier than in the case of the laminar flow. The reflected shock wave in the laminar flow can be visualized in Fig. 13 as a sharp contour concentration in the middle of the duct passage at the entrance of the exhaust flow, while it is not visible in Fig. 14 for the turbulent result.

Wall-pressure distributions are depicted in Figs. 15–17 for $M_\infty = 10.1$, 13.2, and 14.9, respectively. As seen previously for $M_\infty = 12$, laminar and turbulent results do not differ

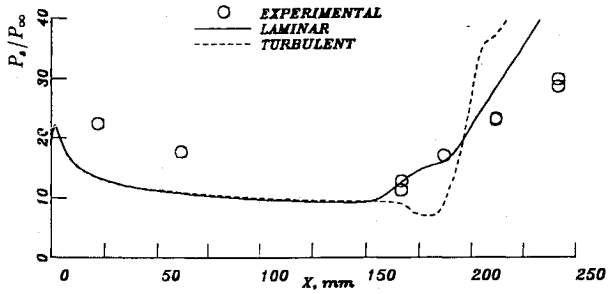

Fig. 17 Centerbody pressure, 145 × 125, M = 14.9.

Fig. 18 Mach number contours, laminar, M = 10.1.

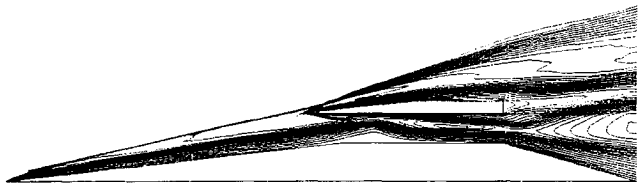

Fig. 19 Mach number contours, laminar, M = 13.2.

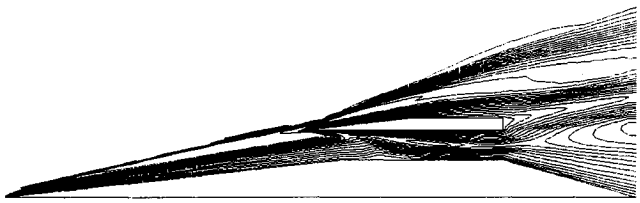

Fig. 20 Mach number contours, turbulent, M = 14.9.

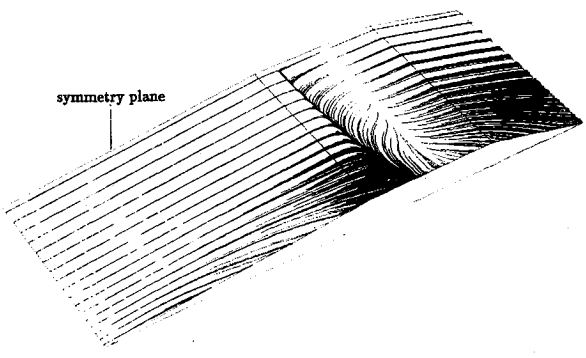

Fig. 21 Particle traces, M = 12.

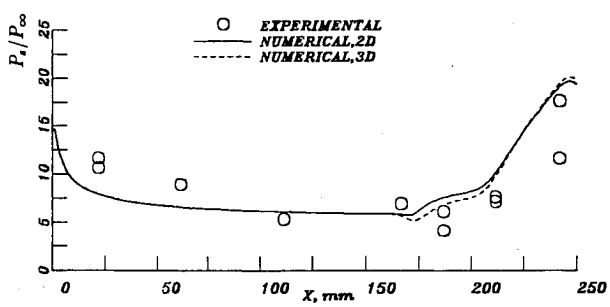

Fig. 22 Centerbody pressure, two-dimensional and three-dimensional comparison, M = 12.

significantly on most of the ramp surface, but start to show considerable differences at a location where the upstream influence from the interaction is experienced. All turbulent results have a drop in pressure across the expansion corner and a rather high pressure rise behind the shock. The best agreement with experimental data is achieved for the laminar flow at the Mach number of 10.1. The pressure rise behind the shock for this particular case seems to be the most consistent in all cases. For M_∞ = 14.9, laminar solutions also agree with the measurement better near the interaction than the turbulent results. Disagreement is large near the leading edge for M_∞ = 14.9 as shown in Fig. 17.

Clearly, computed turbulent results appear underpredicting the flow characteristics near the interaction, such as much smaller regions of reversed flows, and higher pressure rises behind the shock. One of the important factors for the underprediction may be attributed to the lack of compressibility effects in the present turbulent model, as mentioned before. Numerically, without this correction, the model can give large values of eddy viscosity, especially at high Mach numbers, resulting in a bigger amount of turbulent diffusion that can smooth out sharp viscous gradients created by the interaction, consequently contributing to the discrepancy.

Figures 18–20 show the Mach number contours for laminar flows at M_∞ = 10.1 and 13.2, and for turbulent flows at M_∞ = 14.9. It should be noted that the thickness of the laminar and turbulent boundary layers remains essentially the same on the ramp because of the effect of low density that gives low Reynolds numbers. The most important observation that can be made from Figs. 18–20 is that the ramp boundary layer is significantly thickening as the Mach number increases, whether the flow is laminar or turbulent. These effects described above and other viscous effects within the duct passage produced by the boundary-layer's growth, such as massive separation, become even more severe at higher Mach numbers.

Finally, flowfields for the three-dimensional model for a laminar flow are calculated to study any three-dimensional effect that may exist. Figure 21 shows particle traces on a vertical grid plane adjacent to the centerbody surface from the results for M_∞ = 12. As seen from this figure, the flow has a three-dimensional nature evidenced by the spanwise turning of the flow beginning at the ramp leading edge, but the flow three dimensionality is significant only in regions along the edge of the model. The relieved spillage effect exists because the ambient pressure is lower than the centerbody surface pressure and it generates a secondary flow with a spanwise velocity component. The regions showing this secondary flow become more and more visible downstream. The separation region also shows the three dimensionality as suggested by the downstream bending of the separation line near the edge. There is a difference in pressure between two-dimensional and three-dimensional flows near the interaction due to the effect of three dimensionality that reduces the zone of upstream influence, but the effect is small as shown in Fig. 22.

Summary

Results for a scramjet model have been presented in a series of numerical simulations in two and three dimensions at several hypersonic Mach numbers. The primary difficulty has been the ability to accurately predict the flow structure of the interaction between a shock wave and a thick boundary layer at low Reynolds numbers. Although there is some improvement observed, grid refinement and turbulence model without compressibility do not consistently improve the results. In general, the effect of the fine grid tends to overpredict the zone of upstream influence, while the effect of turbulence is to underpredict this zone. It is uncertain whether the flow is laminar or turbulent from the present calculations, and other models with a compressibility correction should be considered for this purpose and solution improvement in future study.

With the present inlet configuration at high Mach number, the ramp viscous layer grows considerably and occupies a large portion of the duct passage. While there are large disagreements between the present solutions and the experimental data near the leading edge, the calculated wall pressure near the end of the inlet ramp agrees relatively well with the experimental data. The large difference between the present results and the experimental data near the leading edge may be due to the numerical and/or experimental uncertainty, but cannot be explained in the present study. The computation of the full three-dimensional model yields better agreements between the calculated pressure and experimental data near the interaction and separation regions than the two-dimensional computation does.

Acknowledgments

This work was supported by the NASA Lewis Research Center under Contracts NAS3-24105 and NAS3-25266 with D. R. Reddy as monitor.

References

[1]Reddy, D. R., Smith, G. E., Liou, M. F., and Benson, T. J., "Three-Dimensional Viscous Analysis of a Hypersonic Inlet," AIAA Paper 89-0004, Jan. 1989.

[2]Duncan, B., "CFD Analysis of a Hydrogen Fueled Ramjet Engine at Mach 3.44," AIAA Paper 91-1991, June 1991.

[3]Minucci, M., and Nagamatsu, H., "Experimental Study of a Two-Dimensional Scramjet Inlet, $M_\infty = 10.1-25.1$," *Journal of Propulsion and Power*, Vol. 8, No. 3, 1992, pp. 680–686.

[4]Minucci, M., and Nagamatsu, H., "Investigation of a 2D Scramjet Inlet, $M_\infty = 8-18$ and $T_0 = 4100$ K," *Journal of Propulsion and Power*, Vol. 9, No. 1, 1993, pp. 139–145.

[5]Lai, H., and Nelson, E., "Comparison of 3D Computation and Experiment for Non-Axisymmetric Nozzles," AIAA Paper 89-0007, Jan. 1989.

[6]Lai, H. T., "3D Computation of Single-Expansion-Ramp and Scramjet Nozzles," *Computational Fluid Dynamics Symposium on Aeropropulsion*, 1990, pp. 559–571 (NASA CP-10045).

[7]Lai, H. T., "3D Computation of Hypersonic Nozzle," AIAA Paper 90-5203, Oct. 1990.

[8]Pulliam, T. H., "Euler and Thin Layer Navier-Stokes Codes: ARC2D, ARC3D," *Notes for Computational Fluid Dynamics User's Workshop*, Univ. of Tennessee Space Inst., Tullahoma, TN, 1984, pp. 15.1–15.85 (UTSI Pub. E02-4005-023084).

[9]Cooper, G. K., "The PARC Code: Theory and Usage," Arnold Engineering Development Center, AEDC-TR-87-24, 1987.

[10]Baldwin, B. S., and Lomax, H., "Thin Layer Approximation and Algebraic Model for Separated Turbulent Flows," AIAA Paper 78-0257, Jan. 1978.